Article

Binary Type-II Heterojunction K$_7$HNb$_6$O$_{19}$/g-C$_3$N$_4$: An Effective Photocatalyst for Hydrogen Evolution without a Co-Catalyst

Qi Song [†], Shiliang Heng [†], Wenbin Wang, Huili Guo, Haiyan Li and Dongbin Dang *

Henan Key Laboratory of Polyoxometalate Chemistry, College of Chemistry and Chemical Engineering, Henan University, Kaifeng 475004, China; songqi1666@163.com (Q.S.); hengshiliangecnu@163.com (S.H.); wwenbin2022@163.com (W.W.); ghlhenu@163.com (H.G.); lihaiyan@henu.edu.cn (H.L.)

*** Correspondence: dangdb@henu.edu.cn

[†] These authors contributed equally to this work.

Abstract: The binary type-II heterojunction photocatalyst containing g-C$_3$N$_4$ and polyoxoniobate (PONb, K$_7$HNb$_6$O$_{19}$) with excellent H$_2$ production activity was synthesized by decorating via a facile hydrothermal method for the first time. The as-fabricated Nb–CN-0.4 composite displayed a maximum hydrogen evolution rate of 359.89 μmol g^{-1} h^{-1} without a co-catalyst under the irradiation of a 300 W Xenon Lamp, which is the highest among those of the binary PONb-based photocatalytic materials reported. The photophysical and photochemistry analyses indicated that the hydrogen evolution performance could be attributed to the formation of a type-II heterojunction, which could not only accelerate the transfer of photoinduced interfacial charges, but also effectively inhibit the recombination of electrons and holes. This work could provide a useful reference to develop an inexpensive and efficient photocatalytic system based on PONb towards H$_2$ production.

Keywords: PONb-based photocatalyst; g-C$_3$N$_4$; type-II heterojunction; photocatalytic hydrogen evolution

1. Introduction

A looming global energy shortage makes it increasingly urgent to develop environmentally friendly green chemical technology for energy production to ensure the sustainable development of human society [1–3]. In recent decades, much effort has been devoted to developing the production of hydrogen, not merely because it is an important chemical raw material; more importantly, hydrogen energy is recognized as the most ideal and promising clean energy of the future [4]. Due to its environmental friendliness, efficient cost performance and non-polluting nature, photocatalytic technology has been widely used to produce such green energy [5]. Photocatalysis water splitting exhibits a great potential in hydrogen production and is expected to achieve industrialization [6,7]. However, the development of low-cost and highly efficient photocatalysts for hydrogen production is still a major challenge for practical application.

Polyoxometalate (POM) is a kind of metal oxide cluster based mainly on Mo, W, V, Nb and Ta elements [8], which have been widely studied due to their promising applications in fields such as water oxidation, hydrogen evolution, carbon dioxide reduction, and nitrogen reduction reaction [9]. As a special subclass of POMs with the unique electronic characteristics of high charge density and rapid electron transfer rate, polyoxoniobates (PONbs) have been employed to assemble photocatalytic composites with other semiconductor species [10]. It is worth mentioning that the Lindqvist type K$_7$HNb$_6$O$_{19}$ is a favorite candidate to be selected to be as a model of PONbs to investigate the construction of PONb-based hydrogen-evolution photocatalysts, for its easy preparation and high stability [11]. However, immobilization and reusability are a tremendous challenge for such materials because of the water solubility, highly alkalinity, and confined working pH region of the components of K$_7$HNb$_6$O$_{19}$ [12,13].

Graphitic carbon nitride (g-C_3N_4, CN) is reported to be a promising photocatalyst for hydrogen evolution because of its appropriate band gap and energy structure being capable of performing water reduction reaction [14,15]. However, the photocatalytic hydrogen production activity of pure g-C_3N_4 is confined by the rapid electron-hole recombination and tardy charge mobility, leading to the low photocatalytic activity [16,17]. A large number of researchers have shown that the photocatalytic activity of g-C_3N_4 can be enhanced by morphology regulation, element doping, dye sensitization, heterojunction construction, various noble metals loading (Pt, Au), and other methods [18–22]. Among them, two strategies of loading noble metals and constructing heterojunctions have been employed widely as effective ways to boost the catalytic property of g-C_3N_4 [23]. Nevertheless, constructing heterojunctions by combining with other semiconductors is a preferred method to fabricate g-C_3N_4-based photocatalysts on account of the high scarcity and cost of noble metals [24]. It was proven that the combination of g-C_3N_4 and POMs is an effective strategy to obtain heterojunctions with improved photoactivity, which not only gives them a large specific surface and a narrowed band gap, but also could accelerate the photoinduced interfacial charge transfer and inhibit effectively the recombination of the electrons and holes in the process of photocatalysis. For example, a series of type II heterojunction composites (POMs/C_3N_4) were reported based on Keggin-type polyoxoanions $SiW_{12}O_{40}^{4-}$, $PW_{12}O_{40}^{3-}$ and $PMo_{12}O_{40}^{3-}$ [25]. Up to now, the reported POM-based g-C_3N_4 hybrid materials such as $Co_4PW_9O_{34}$/g-C_3N_4, $FePW_4O_{24}$/g-C_3N_4 and $PMo_{10}V_2O_{40}$/g-C_3N_4 have mainly been based on acidic POMs [26–28]. As for the highly basic PONbs, there have only been a few examples reported, such as Mg_3Al–LDH–Nb_6, CdS/$K_7HNb_6O_{19}$/NiS, $K_8Nb_6O_{19}$/g-C_3N_4 and $K_4Nb_6O_{17}$/g-C_3N_4 [12,29–31]. In this work, a series of $K_7HNb_6O_{19}$/g-C_3N_4 photocatalysts were fabricated via a facile hydrothermal method, which was used for effective H_2 generation without any co-catalyst. To the best of our knowledge, this is the first study constructing a binary $K_7HNb_6O_{19}$/g-C_3N_4 type-II heterojunction photocatalyst, and it possesses outstanding photocatalytic H_2 evolution properties under ultraviolet light driving.

2. Experimental Section

2.1. Chemicals and Reagents

All chemicals were reagent grade and used without further purification. Niobium pentoxide (Nb_2O_5, AR), methyl alcohol (MeOH, AR), potassium hydroxide (KOH, AR), sodium sulfate (Na_2SO_4, AR), ethanol (EtOH, AR) and urea ($CO(NH_2)_2$, AR) were purchased from Sinopharm Chemical Reagent Co., Ltd. (Shanghai, China).

2.2. Synthesis of $K_7HNb_6O_{19}\cdot13H_2O$

$K_7HNb_6O_{19}\cdot13H_2O$ was synthesized according to the method reported in the literature [32]. Typically, 13.3 g Nb_2O_5 and 26 g KOH were added into the nickel crucible and mixed evenly. The resultant mixture was heated in a muffle furnace at 480 °C for 50 min; then the product was collected and dissolved in 100 mL boiling water after it was cooled to room temperature. When the volume of the solution reached about 50 mL by evaporating water, the heating was stopped. The white solids were collected and dried in vacuum.

2.3. Synthesis of g-C_3N_4

The g-C_3N_4 was prepared through the direct calcination of urea according to the methods reported in the literature [33]. Typically, urea was placed evenly in a covered crucible and heated at 550 °C for 3 h in a tube furnace, with a heating rate of 10 °C min^{-1}. The resultant product was taken out when the temperature cooled to about 30 °C and then ground for use.

2.4. Synthesis of Nb–CN-X Composites

Nb–CN-*X* composite photocatalysts were prepared according to the following process, where *X* refers to the mass of g-C_3N_4 added based on 1 g $K_7HNb_6O_{19}$ as a benchmark;

X = 0.2, 0.4, 0.6, 0.8. Typically, taking Nb–CN-0.4 as an example, as-obtained 0.4 g g-C_3N_4 was added to a solution containing 1 g Linquist type $K_7HNb_6O_{19}$ and 15 mL deionized water and stirred for 3 h to form yellow mixed suspension, and then it was transferred to a 25 mL Teflon-lined reactor and heated at 180 °C for 12 h. The resulting precipitate was collected and washed separately with high-purity water and ethanol three times and then dried in a vacuum oven at 60 °C for 12 h to obtain the white photocatalyst Nb–CN-0.4 composite. Similarly, other composites were also synthesized by adjusting the amount of g-C_3N_4 (X = 0.2, 0.6, 0.8) according to the same process. The preparation process is shown in Figure 1. The detailed characterization methods and analytical methods are described in the Supporting Information.
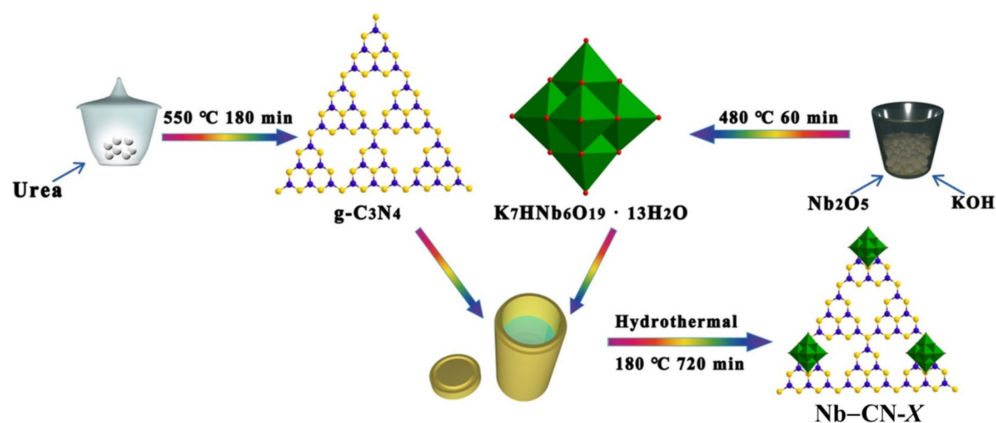

Figure 1. Schematic illustration of the fabrication of Nb–CN-X composites.

3. Results and Discussion

3.1. Morphology and Structure Analysis

The crystalline phase of the as-prepared $K_7HNb_6O_{19}$, g-C_3N_4 and Nb–CN-X composites were characterized by X-ray diffraction (XRD). As shown in Figure 2, the diffraction peaks of pure g-C_3N_4 are 13.3° and 27.5°, while the original $K_7HNb_6O_{19}$ has sharp diffraction peaks at 9.8°, 26° and 48°, which is consistent with the reported results [30,34]. There are three distinct characteristic peaks located at the positions of 8.8°, 27.5° and 46° for Nb–CN-X composites. Among them, the peak at 27.5° matches with the (002) crystal plane of g-C_3N_4, indicating that g-C_3N_4 has been successfully introduced. However, the diffraction peak corresponding to the (100) crystal plane of g-C_3N_4 at 13.3° cannot be observed clearly in the Nb–CN-X composites with the introduction of $K_7HNb_6O_{19}$, which may be due to the low content of g-C_3N_4. Concurrently, the sharp XRD pattern signals from the polyoxoniobate are not visible in the binary composites, while two new wide peaks at 8.8° and 46° are observed, which could be attributed to the peaks of $K_7HNb_6O_{19}$ shifted from 9.8° and 48°. This phenomenon might be caused by the coupling between the two components $K_7HNb_6O_{19}$ and g-C_3N_4 in the composites [35]. In addition, with the increasing of the content of g-C_3N_4 in the Nb–CN-X composites, the peak intensity of $K_7HNb_6O_{19}$ decreased little by little, while that of g-C_3N_4 increased gradually, showing the successful composite of the two components in Nb–CN-X.

To give the further information of the composite photocatalysts, the FT-IR spectra of the $K_7HNb_6O_{19}$, g-C_3N_4 and Nb–CN-0.4 composite were carried out as representatives. As shown in Figure 3, for Nb–CN-0.4 composite, the three vibrational absorption peaks observed at 853, 674 and 530 cm^{-1} belonged to the tensile vibration of Nb–O and Nb–O–Nb of $K_7HNb_6O_{19}$ [24,36]. The characteristic peaks of g-C_3N_4 in Nb–CN-0.4 appeared at different wavebands in the absorption region. The wide peak between 3000 and 3600 cm^{-1} was caused by the stretching vibration of N–H and O–H of the physical absorption water molecules [37]. The peaks at 1630 cm^{-1} are attributed to the stretching vibration of C=N in g-C_3N_4, while the peaks at 1405, 1321, 1246 and 807 cm^{-1} belonged to a typical C–N heterocyclic stretching vibration for triazinyl units [23,38]. Combined with the results

of XRD and FT-IR, the conclusion can be drawn that under hydrothermal conditions, $K_7HNb_6O_{19}$ was successfully embedded in g-C_3N_4, rather than simply mixed, to form the final hybrid material Nb–CN-0.4 composite.
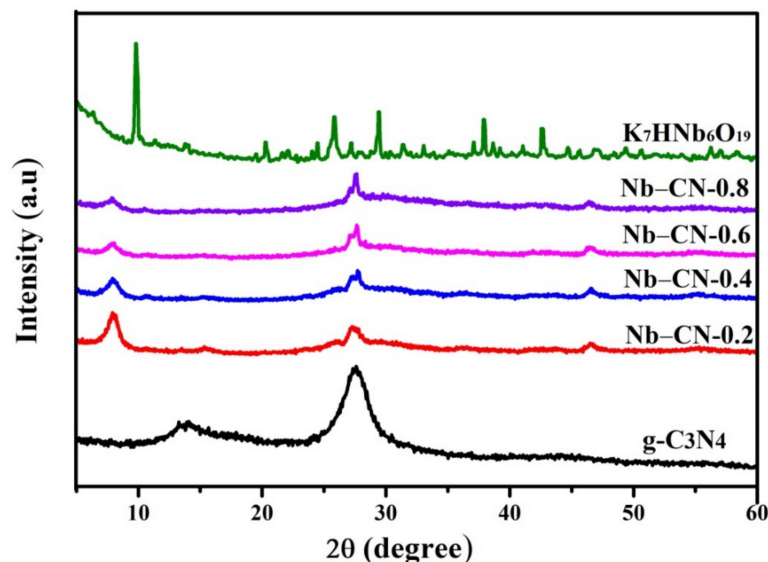

Figure 2. XRD patterns of g-C_3N_4, $K_7HNb_6O_{19}$ and Nb–CN-*X* composites (*X* = 0.2, 0.4, 0.6, 0.8).
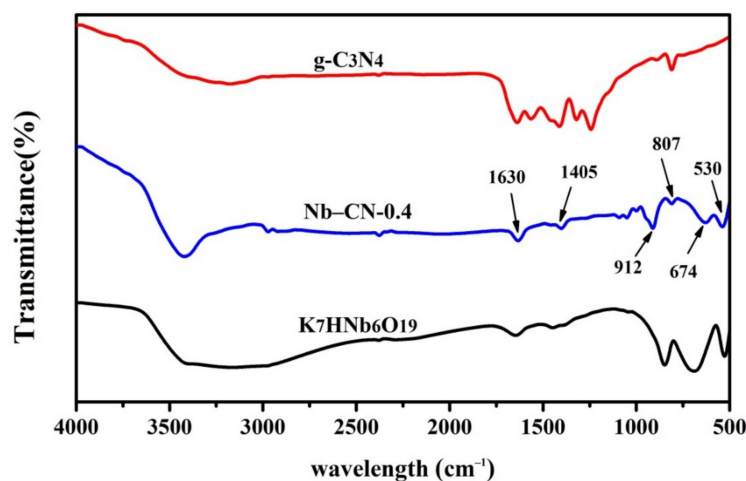

Figure 3. FT-IR spectra of pure g-C_3N_4, $K_7HNb_6O_{19}$ and Nb–CN-0.4 composite.

The morphology and structures of photocatalysts $K_7HNb_6O_{19}$, g-C_3N_4 and Nb–CN-0.4 composite were investigated by SEM, TEM and mapping techniques. It is generally known that the Lindqvist type $K_7HNb_6O_{19}$ is made up of six co-planer Nb–O octahedrons to form a super octahedron, as shown in Figure S1, leading to a highly symmetric compact structure [39]. Figures 4a and S2 reveal that the pure $K_7HNb_6O_{19}$ showed a transparent rodlike morphology. The pure g-C_3N_4 obtained by annealing urea exhibited a large piled sheet shape (Figure 4b), which was caused by thermal polycondensation of urea [40]. The SEM image of Nb–CN-0.4 composite (Figure 4c) presented a thin nanosheet morphology, just like that of the pure g-C_3N_4 but with better dispersion. However, $K_7HNb_6O_{19}$ couldn't be observed in the SEM image, maybe due to its highly uniform distribution caused by the good solubility of $K_7HNb_6O_{19}$ under hydrothermal conditions. To further confirm the existence of $K_7HNb_6O_{19}$, element mapping was performed. As shown in Figure 5, C, O, Nb, K and N elementals were distributed uniformly, further proving the formation of the heterogeneous structure containing $K_7HNb_6O_{19}$ and g-C_3N_4. Exposing the individual components (pristine g-C_3N_4 and $K_7HNb_6O_{19}$) to the hydrothermal condition is of impor-

tance in order to verify the reason causing morphology changes of the achieved composite catalysts in the hydrothermal process. Therefore, we treated the individual component $K_7HNb_6O_{19}$ at 180 °C for 12 h, and found it was still a clear and transparent aqueous solution. After evaporating, the obtained crystals showed an identical IR to that of the freshly prepared $K_7HNb_6O_{19}$ (Figure S3), indicating that $K_7HNb_6O_{19}$ can exist stably under the hydrothermal condition. For the pristine g-C_3N_4, as seen in Figure S4, the hydrothermal treatment made its morphology change from an original sheet shape to the extremely irregular rodlike shape. Based on the comparison of the morphology of g-C_3N_4 before and after hydrothermal treatment, it can be concluded that the presence of $K_7HNb_6O_{19}$ could positively induce the morphology change of the obtained composite, which is consistent with our previous reports [35,36]. The results of HRTEM measurement showed that the introduction of $K_7HNb_6O_{19}$ made the Nb–CN-0.4 composite possess a more regular ultrathin nanosheet structure compared to that of the pure g-C_3N_4 (Figure 4d–f). Ultimately, a number of nanosheets stacked together to further form a flower-like shape unit of the composite (Figure 4f). For the photocatalyst Nb–CN-0.4 composed of ultrathin nanosheets, an improved charge transfer efficiency could be expected compared with pure $K_7HNb_6O_{19}$ [41], which is consistent with good photocatalytic performance.

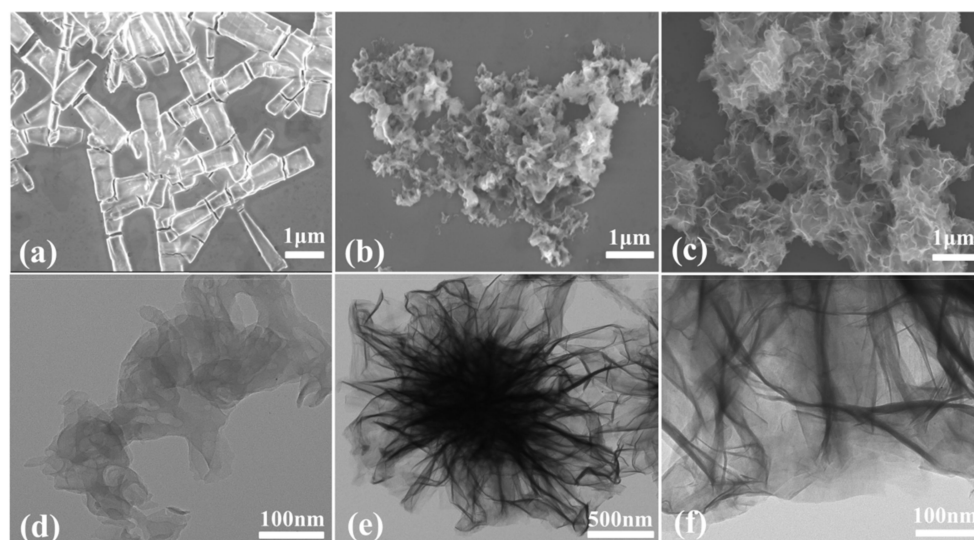**Figure 4.** SEM images of (**a**) $K_7HNb_6O_{19}$, (**b**) g-C_3N_4 and (**c**) Nb–CN-0.4. TEM images of (**d**) g-C_3N_4, (**e**) Nb–CN-0.4 and (**f**) Nb–CN-0.4.
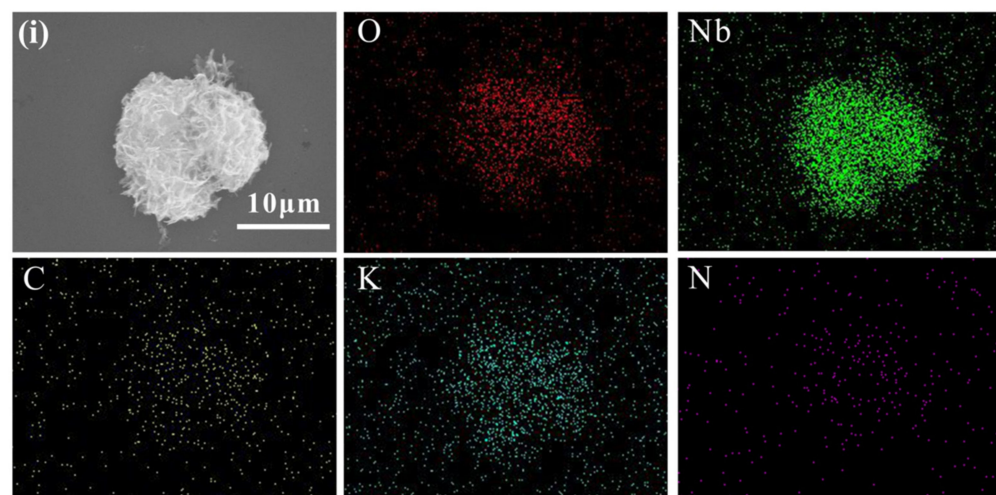

Figure 5. EDS element mapping images for O, Nb, C, K and N of (**i**) Nb–CN-0.4.

The surface chemical status of $K_7HNb_6O_{19}$, g-C_3N_4 and Nb–CN-0.4 composite was studied by X-ray photoelectron spectroscopy (XPS). As shown in Figure S5, the full XPS spectra clearly show the existence of C, Nb, N, K and O elements in the composite sample, indicating that the hybrid material had all the characteristic elements of $K_7HNb_6O_{19}$ and g-C_3N_4. In the C 1s spectrum (Figure 6A), the main characteristic peak centered at 284.8 eV could be attributed to that of sp^2 C–C or C=C bonds, which derived from the amorphous reference carbon on the surface. For the pure g-C_3N_4, the peak centered at 288.3 eV corresponded to the sp^2 carbon atoms bonded to N (N=C–(N)$_2$) in the graphitic structure [42,43]. It should be noted that the C 1s peak centered at 286.2 eV in Nb–CN-0.4 showed a distinct shift toward the lower band energy direction after hydrothermal treatment compared with the pure g-C_3N_4, indicating the presence of strong interactions between the terminal oxygen atom of Nb=O or the bridge oxygen of Nb–O–Nb from $K_7HNb_6O_{19}$ and the N=C–(N)$_2$ group from g-C_3N_4. In addition, the strong electronic pull of the Linqvist anions might also have affected the position of the C 1s peak [30]. The three N 1s peaks in Nb–CN-0.4 composite were observed at the positions 399.8, 400.9 and 401.8 eV, with the intensity slightly greater than those of g-C_3N_4, corresponding to the peaks of sp^2 N atoms involved in tris-triazine rings (C=C–N), tertiary nitrogen (N–(C)$_3$) and N atoms bonded with H atoms (C–N–H) in the aromatic rings, respectively [44]. It can be seen from Figure 6c that three peaks, centered at 528.9, 530.6 and 531.9 eV, were observed on the $K_7HNb_6O_{19}$ sample, which were assigned to Nb–O–Nb, Nb–O–H and adsorbed water, respectively [24]. After hydrothermal treatment, the O 1s in Nb–CN-0.4 had two main peaks, of which the peak at 532.1 eV was adsorbed water, while the other one resulted from the binding energy of different oxygen-containing species. Compared with the pure $K_7HNb_6O_{19}$, the binding energy peaks located at 206.8 and 209.5 eV corresponded to Nb $3d_{5/2}$ and $3d_{3/2}$ in the Nb–CN-0.4 composite, which indicates that Nb is in its highest oxidation state (+5 valence state) [24] (Figure 6d), and the shift of Nd 3d binding energy further confirmed that there was an interaction between the Lindqvist unit of the $K_7HNb_6O_{19}$ sample and g-C_3N_4 sample. Figure S6 shows that K 2p binding energies did not change significantly in $K_7HNb_6O_{19}$ and the composite, except for their intensities.
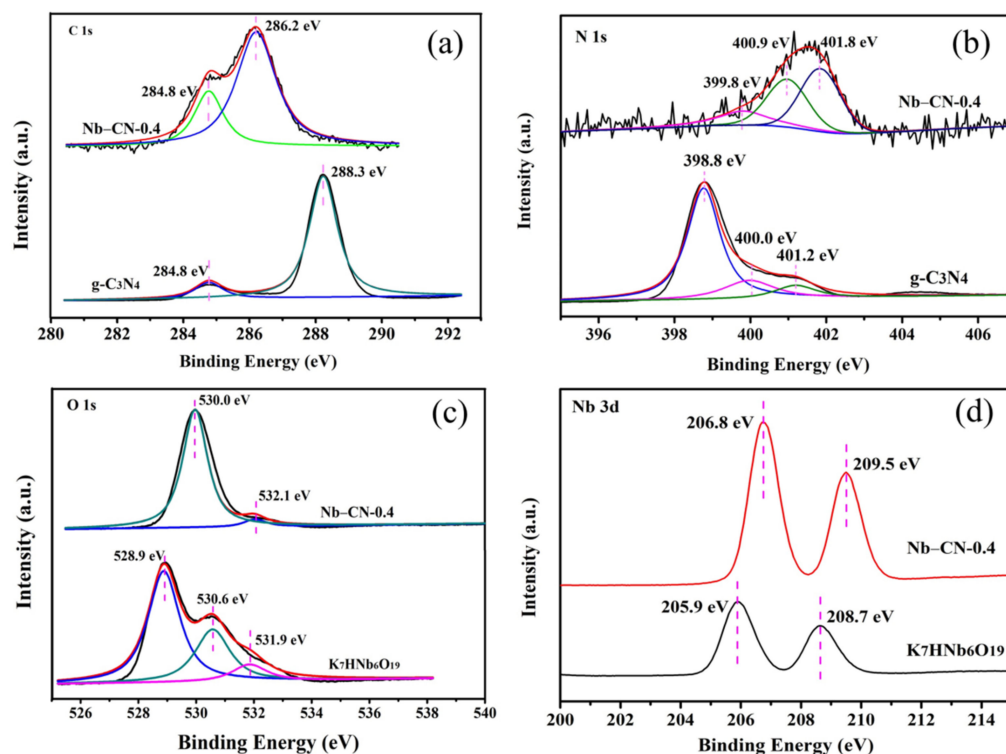

Figure 6. High resolution XPS spectra of $K_7HNb_6O_{19}$, Nb–CN-0.4 composite and g-C_3N_4: (**a**) C 1s; (**b**) N 1s; (**c**) O 1s; (**d**) Nb 3d.

The BET tests of $K_7HNb_6O_{19}$, g-C_3N_4 and Nb–CN-0.4 composite were carried out, and the N_2 adsorption–desorption isotherms are shown in Figure S7. The calculated specific surface areas of $K_7HNb_6O_{19}$ and g-C_3N_4 were about 3.15 m^2 g^{-1} and 52.13 m^2 g^{-1}, respectively, while that of Nb–CN-0.4 composite increased to 55.34 m^2 g^{-1} after the introduction of g-C_3N_4. The larger specific surface area is conducive to the enhancement of the photocatalytic activity [45], which would promote more water molecule adsorption on the surface of the catalysts. Meanwhile, it is also beneficial for the increase of catalytic active sites.

3.2. Optical and Electric Properties

Raman spectroscopy of $K_7HNb_6O_{19}$, g-C_3N_4 and Nb–CN-0.4 composite are depicted in Figure 7. There were two obvious peaks at 759 and 901 cm^{-1} for Nb–CN-0.4 composite, which were attributed to the terminal oxygen and bridging oxygen in $K_7HNb_6O_{19}$ [46]. The broad band in 400–700 cm^{-1} was attributed to g-C_3N_4 in Nb–CN-0.4 composite. As for the pure g-C_3N_4, the Raman peaks located at 592 cm^{-1}, 725 cm^{-1}, 1055 cm^{-1}, 1165 cm^{-1}, 1296 cm^{-1}, 1441 cm^{-1} and 1550 cm^{-1} were related to CN heterocyclic stretching vibration, of which the last two in the high wavenumber region were attributed to D and G bands of g-C_3N_4 of a typical graphitic structure, respectively [47,48]. Compared to the bare $K_7HNb_6O_{19}$ and g-C_3N_4, the Raman peaks of Nb–CN-0.4 composite became broader, further proving the formation of the hybrid material and matching well with the results of IR and X-ray powder diffraction analysis.
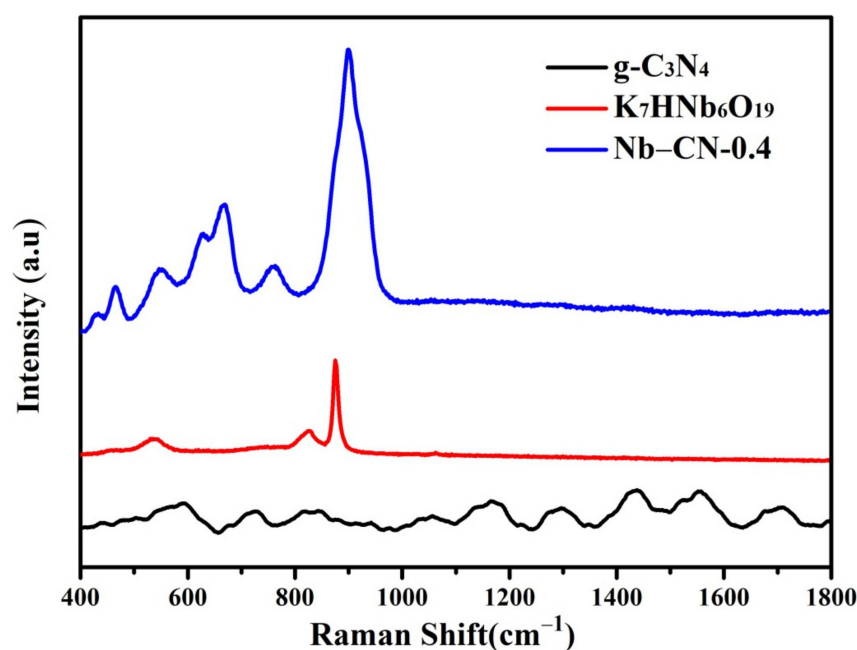

Figure 7. Raman spectra of $K_7HNb_6O_{19}$, g-C_3N_4 and Nb–CN-0.4 composite.

The optical absorption properties of photocatalysts $K_7HNb_6O_{19}$, g-C_3N_4 and Nb–CN-*X* composites were characterized by UV-vis DRS (Figure S8). As shown in Figures S6 and 8a, $K_7HNb_6O_{19}$ only absorbed ultraviolet light, and the absorption edge was about 310 nm, while all the composites showed a slightly broader absorption after introducing C_3N_4, which was undoubtedly attributed to the contribution of g-C_3N_4 with the absorption band edge around 450 nm [49]. The band gap values of as-prepared photocatalysts were calculated according to the equation of $(\alpha h v)^2 = A(h v - E_g)$, where α, h, v and A represent the absorption coefficient, Plank constant, light frequency and a constant, respectively [50]. As described in Figure 8b, the band gap value E_g of the pure $K_7HNb_6O_{19}$ and g-C_3N_4 were about 3.98 and 2.73 eV, respectively, which were consistent with literature reports [29,51]. The E_g value of Nb–CN-0.4 was about 3.42 eV, slightly narrower than that of $K_7HNb_6O_{19}$,

indicating the presented composite is an ultraviolet light photocatalyst without activity under visible light irradiation.

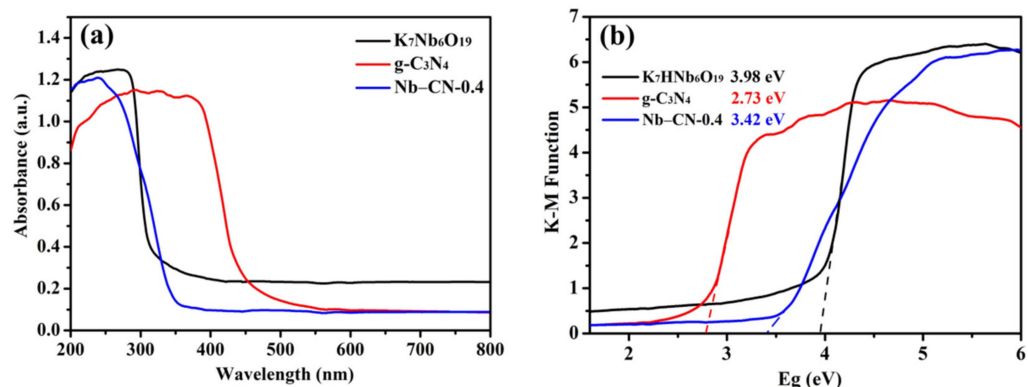**Figure 8.** (**a**) UV−visible absorbance spectra of $K_7HNb_6O_{19}$, g-C_3N_4 and Nb–CN-0.4 composite; (**b**) Kubelka−Munk transformed reflectance spectra of $K_7HNb_6O_{19}$, g-C_3N_4 and Nb–CN-0.4 composite.

To study the separation efficiency of the photogenerated carriers of the samples, photoluminescence spectroscopies (PL) of g-C_3N_4 and Nb–CN-0.4 composite were performed. The fluorescence intensity of each sample was studied at the same excitation wavelength of 300 nm. Generally, a lower PL intensity indicates a lower recombination rate of the photoexcited electrons and holes, meaning a higher photocatalytic activity [52]. As shown in Figure S9, the introduction of $K_7HNb_6O_{19}$ can partially quench the fluorescence of g-C_3N_4, which means that the introduction of $K_7HNb_6O_{19}$ promotes the separation of photogenerated carriers, which is consistent with its good photocatalytic hydrogen production activity.

The photocurrent transient response experiment (Figure 9a) showed that the Nb–CN-0.4 had the highest photocurrent intensity, much higher than the original g-C_3N_4 and $K_7HNb_6O_{19}$, implying that Nb–CN-0.4 had the faster transfer efficiency and more efficient separation of photogenerated charges [53]. Moreover, the electrochemical impedance spectroscopy Nyquist plot was used to analyze the charge transfer rate (Figure 9b). The smallest arc radius of Nb–CN-0.4 under the same test conditions implied that it had the highest separation and migration rate of the photo-generated carriers [54], which was in keeping with the results of photocurrent response and photocatalytic performance studies.
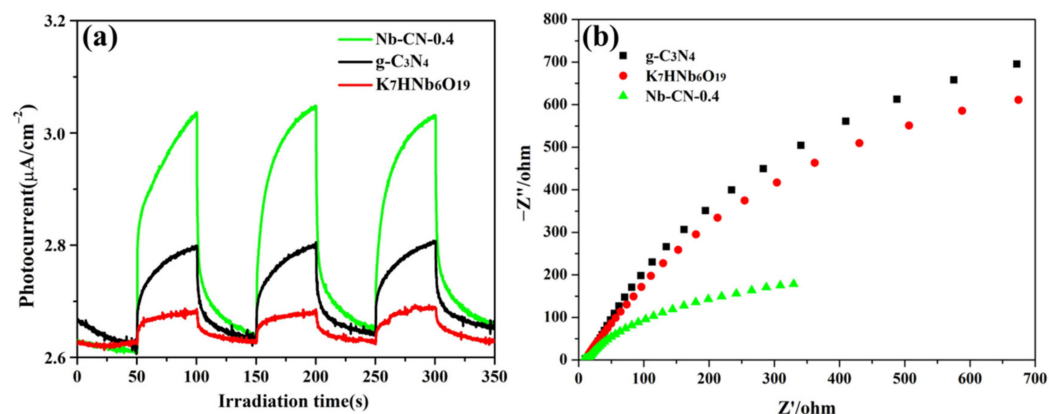
Figure 9. (**a**) Photocurrent response of $K_7HNb_6O_{19}$, g-C_3N_4 and Nb–CN-0.4 composite. (**b**) Electrochemical impedance spectroscopy of g-C_3N_4, $K_7HNb_6O_{19}$ and Nb–CN-0.4 composite.

3.3. Photocatalytic H_2 Production

The photocatalytic performance of hydrogen production of $K_7HNb_6O_{19}$, g-C_3N_4 and Nb–CN-X composites was tested using methanol (MeOH) as a sacrificial agent under a 300 W Xenon Lamp without a co-catalyst. Herein, methanol was selected as the sacrificial

agent because it could act mainly and preferentially as a hole scavenger to decrease the recombination rate of photogenerated charge carriers for enhanced photocatalytic H_2 evolution efficiency, similar to our previous work [35,55]. Typically, 50 mg photocatalyst powder was added into the mixed solution of 40 mL deionized water and 10 mL methanol, and then stirred and sonicated for 15 min to ensure the uniform dispersion of the catalyst; the concentration of the solid catalyst was 1mg/mL. As shown in Figure 10, the average hydrogen evolution rates were 2.72 μmol g^{-1} h^{-1} for $K_7HNb_6O_{19}$ and 9.05 μmol g^{-1} h^{-1} for g-C_3N_4. After combining $K_7HNb_6O_{19}$ with g-C_3N_4, Nb–CN-0.4 composite exhibited the highest hydrogen production rate, as much as 359.89 μmol g^{-1} h^{-1}, approximately 133 and 40 times of the original $K_7HNb_6O_{19}$ and g-C_3N_4, respectively. To the best of our knowledge, the maximum rate of hydrogen production reported is 207.6 μmol h^{-1} g^{-1} for such kinds of photocatalytic materials in the literature (Table S1). Therefore, Nb–CN-0.4 composite represented the binary PONb-based photocatalytic material with the highest hydrogen production rate up to now. Figure 10b showed that with the amount of g-C_3N_4 increasing, the H_2 producing activity of Nb–CN-X composites increased gradually to a maximum value and then decreased. Although the coupling of $K_7HNb_6O_{19}$ and g-C_3N_4 could effectively increase the hydrogen production efficiency and significantly improve the photocatalytic performance, the excessive g-C_3N_4 would bring about a shielding effect and introduce more recombination centers, which was not conducive to the charge separation, leading to a low performance of photocatalytic hydrogen production.
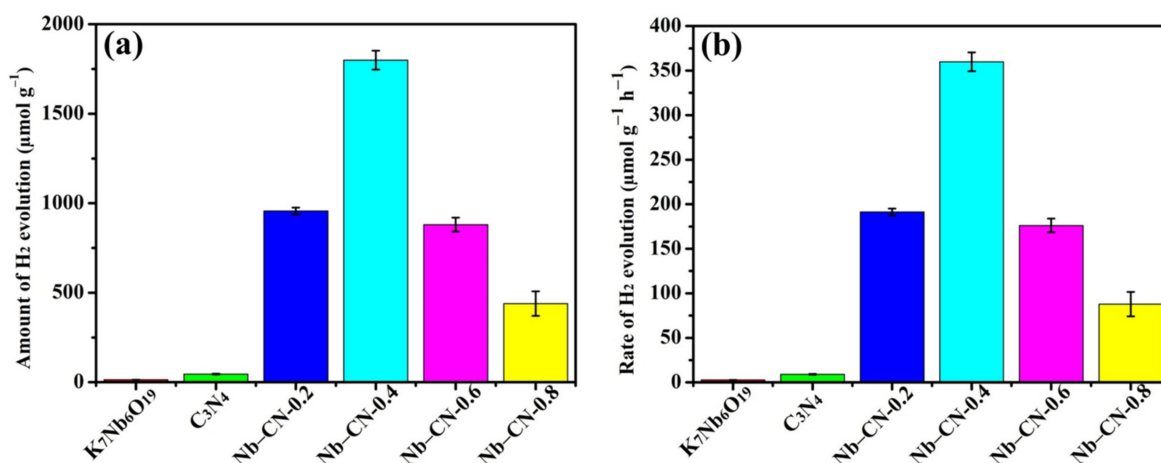

Figure 10. The amount (**a**) and rate (**b**) of H_2 evolution with 5 h of illumination on pure $K_7HNb_6O_{19}$, g-C_3N_4 and Nb–CN-*X* composites.

To verify the stability of the prepared photocatalyst, the recyclability performance of the optimal sample of Nb–CN-0.4 composite was evaluated under the same condition. As shown in Figure 11a, after four recycling experiments, the hydrogen evolution rate did not decrease obviously, indicative of a high stability of the sample. Moreover, the crystallinity of the catalyst was retained well after four rounds of recycling, which could be drawn from the XRD pattern in Figure 11b, further proving the good structural and catalytic stability of the prepared composite.

3.4. Investigation of Photocatalytic Mechanism

The valence band XPS spectra test was carried out to study the photocatalytic mechanism (Figure S10). The estimated valence band (VB) positions of $K_7HNb_6O_{19}$ and g-C_3N_4 were 3.61 and 1.67 eV vs. NHE, respectively, which were consistent with the reported values [36]. The conductance band (CB) positions (E_{CB}) of $K_7HNb_6O_{19}$ and g-C_3N_4 were calculated to be −0.37 and −1.06 eV vs. NHE based on the empirical formula of $E_g = E_{VB} - E_{CB}$. Based on the above analysis and the photocatalytic experimental results, we proposed a possible mechanism of photocatalytic hydrogen production, as seen in Figure 12. On

the basis of the definition of a heterojunction [56], a type-II heterojunction photocatalytic system could be formed between $K_7HNb_6O_{19}$ and g-C_3N_4 due to a staggered band gap. Under the full spectral irradiation, the electrons were excited from VB to CB of both g-C_3N_4 and $K_7HNb_6O_{19}$. Because the CB potential of g-C_3N_4 was lower than that of $K_7HNb_6O_{19}$, the photo-induced electrons on the CB of g-C_3N_4 could migrate more easily to the CB of $K_7HNb_6O_{19}$, while the photo-induced h^+ were concentrated on the VB of g-C_3N_4 simultaneously. For the photocatalytic H_2 production, the electrons accumulated on the CB of $K_7HNb_6O_{19}$ could be captured by H^+ to produce H_2, and the holes in the VB of g-C_3N_4 were consumed by the sacrificial agent CH_3OH. The mechanism of photocatalytic hydrogen evolution is shown in Figure 12, and the pathways can be illustrated as follows:

$$Nb\text{-}CN\text{-}X + h\upsilon \rightarrow Nb\text{-}CN\text{-}X + e^- + h^+ \tag{1}$$

$$e^- + 2H^+ \rightarrow H_2 \tag{2}$$

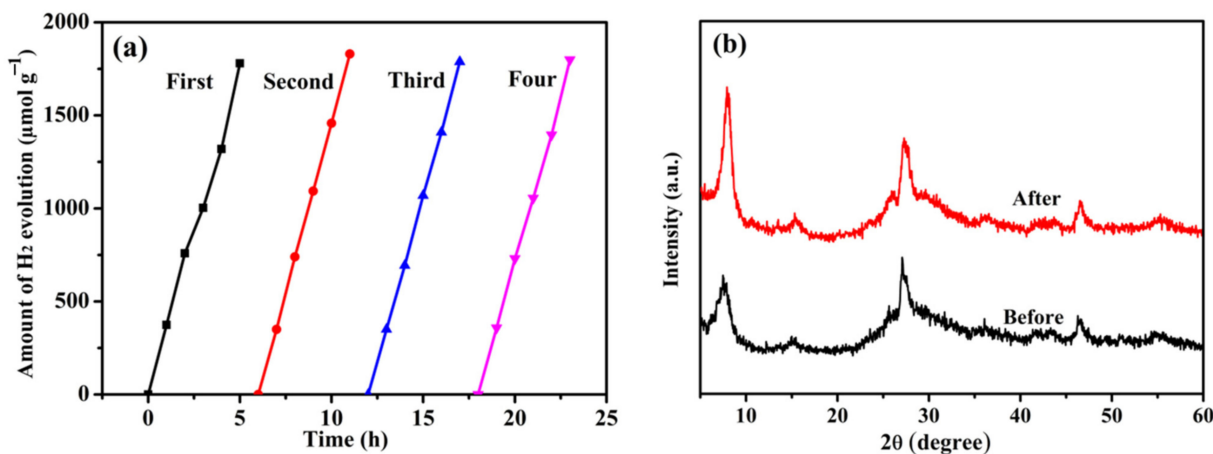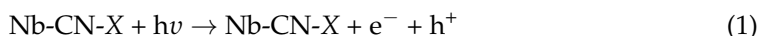$$h^+ + CH_3OH \rightarrow CH_3OH^+ \tag{3}$$

Figure 11. (**a**) Nb–CN-0.4 composite hydrogen production cycle effect; (**b**) XRD patterns of Nb–CN-0.4 composite before and after four cycle tests.
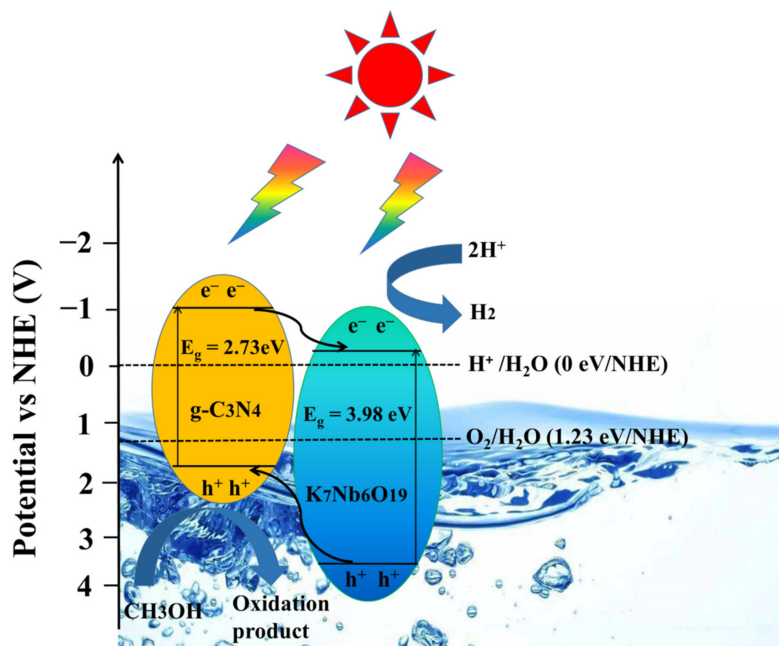

Figure 12. The possible photocatalytic mechanism of type-II heterojunction photocatalyst Nb–CN-0.4 composite hydrogen production.

4. Conclusions

In summary, a series of binary type-II heterojunction Nb–CN-*X* composites were successfully prepared via a one-step hydrothermal method. The obtained optimal photocatalyst Nb–CN-0.4 composite displayed superior photocatalytic H_2 generation activity, with a H_2 generation rate of 359.89 μmol g^{-1} h^{-1}. The binary type-II heterojunction photocatalyst containing g-C_3N_4 and polyoxoniobate (PONb, $K_7HNb_6O_{19}$) with excellent H_2 production activity under ultraviolet light driving was synthesized by decorating via a facile hydrothermal method for the first time and without any co-catalyst, which was approximately 133 and 40 times than that of bare $K_7HNb_6O_{19}$ and g-C_3N_4. The enhanced photocatalytic hydrogen evolution was ascribed to a good heterojunction formed between $K_7HNb_6O_{19}$ and g-C_3N_4, which significantly accelerated the charge carries transfer rate on the interface and improved the separation of photogenerated electrons and holes, as demonstrated by the result of photochemical tests. It is worth mentioning that Nb–CN-*X* composites are the first example of binary type-II heterojunction $K_7HNb_6O_{19}$/g-C_3N_4 photocatalyst to H_2 evolution. This work could provide reference for the preparation and modification of PONb-based photocatalysts with low cost and high performance, as well as their further application in clean energy.

Supplementary Materials: The following supporting information can be downloaded at: https://www.mdpi.com/article/10.3390/nano12050849/s1, Figure S1: Configuration of Lindqvist type $K_7HNb_6O_{19}$, green sphere is Nb, red sphere is oxygen. Figure S2: SEM of $K_7HNb_6O_{19}$. Figure S3: IR of $K_7HNb_6O_{19}$ before and after hydrothermal. Figure S4: SEM of individual component g-C_3N_4 (a) Before hydrothermal treatment (b) After hydrothermal treatment. Figure S5: XPS of g-C_3N_4, $K_7HNb_6O_{19}$ and Nb–CN-0.4 composite in the survey spectra. Figure S6: High resolution K 2p XPS of the pure $K_7HNb_6O_{19}$ and Nb–CN-0.4 composite. Figure S7: N_2 adsorption-desorption isotherms of $K_7HNb_6O_{19}$ and Nb–CN-0.4 composite. Figure S8: UV–vis DRS spectra of Nb–CN-*X* composites. Figure S9: PL spectra of g-C_3N_4 and Nb–CN-0.4 composite. Figure S10: Valence band XPS spectra of $K_7HNb_6O_{19}$, g-C_3N_4. Table S1: Hydrogen production activities of the binary polyoxoniobates materials reported. References [57–61] are cited in the Supplementary Materials.

Author Contributions: Conceptualization, D.D.; Data curation, Q.S.; Formal analysis, H.G.; Funding acquisition, D.D.; Investigation, Q.S. and S.H.; Methodology, S.H., W.W. and H.L.; Project administration, D.D.; Software, S.H., W.W. and H.L.; Supervision, D.D.; Visualization, Q.S.; Writing—original draft, Q.S.; Writing—review and editing, D.D. All authors have read and agreed to the published version of the manuscript.

Data Availability Statement: Data is contained within the article or Supplementary Materials.

Conflicts of Interest: The authors declare no conflict of interest.

References

1. Yi, M.; Wang, X.; Jia, Y.; Chen, X.; Li, C. Titanium dioxide-based nanomaterials for photocatalytic fuel generations. *Chem. Rev.* **2014**, *114*, 9987–10043. [CrossRef]
2. Hou, H.; Zhang, X. Rational design of 1D/2D heterostructured photocatalyst for energy and environmental applications. *Chem. Eng. J.* **2020**, *395*, 125030. [CrossRef]
3. Yi, H.; Huang, D.; Zeng, G.; Cui, L.; Lei, Q.; Min, C.; Ye, S.; Song, B.; Ren, X.; Guo, X. Selective prepared carbon nanomaterials for advanced photocatalytic application in environmental pollutant treatment and hydrogen production. *Appl. Catal. B Environ.* **2018**, *239*, 408–424. [CrossRef]
4. Sołowski, G.; Shalaby, M.S.; Abdallah, H.; Shaban, A.M.; Cenian, A. Production of hydrogen from biomass and its separation using membrane technology. *Sust. Energ. Rev.* **2019**, *82*, 3152–3167. [CrossRef]
5. Yan, J.; Verma, P.; Kuwahara, Y.; Mori, K.; Yamashita, H. Recent Progress on Black Phosphorus-Based Materials for Photocatalytic Water Splitting. *Small Methods* **2018**, *2*, 1800212. [CrossRef]
6. Ng, B.; Putri, L.; Kong, X.; Teh, Y.; Pasbakhsh, P.; Chai, S. Z-Scheme Photocatalytic Systems for Solar Water Splitting. *Adv. Sci.* **2019**, *7*, 1903171. [CrossRef]

7. Nasir, M.S.; Yang, G.; Ayub, S.; Wang, X.; Yan, W.; Peng, S. Ramakrishna, Recent development in graphitic carbon nitride based photocatalysis for hydrogen generation. *Appl. Catal. B Environ.* **2019**, *257*, 117855. [CrossRef]

8. Li, N.; Liu, J.; Dong, B.; Lan, Y. Polyoxometalate-Based Compounds for photo/electrocatalytic applications. *Angew. Chem. Int. Ed.* **2020**, *59*, 20779–20793. [CrossRef] [PubMed]

9. Horn, M.; Singh, A.; Alomari, S.; Goberna-Ferro'n, S.; Vilau, R.; Chodankar, N.; Motta, N.; Ostrikov, K.; MacLeod, J.; Sonar, P.; et al. Polyoxometalates (POMs): From electroactive clusters to energy materials. *Energy Environ. Sci.* **2021**, *14*, 1652–1700. [CrossRef]

10. Zhao, H.; Li, Y.; Zhao, J.; Wang, L.; Yang, G. State-of-the-art advances in the structural diversities and catalytic applications of polyoxoniobate-based materials. *Coordin. Chem. Rev.* **2021**, *440*, 213966. [CrossRef]

11. Xu, Q.; Niu, Y.; Wang, G.; Li, Y.; Zhao, Y.; Singh, V.; Niu, J.; Wang, J. Polyoxoniobates as a superior Lewis base efficiently catalyzed Knoevenagel Condensation. *Mol. Catal.* **2018**, *453*, 93–99. [CrossRef]

12. Dong, J.; Lv, H.; Sun, X.; Wang, Y.; Ni, Y.; Zou, B.; Zhang, N.; Yin, A.; Chi, Y.; Hu, C. A Versatile Self-Detoxifying Material Based on Immobilized Polyoxoniobate for Decontamination of Chemical Warfare Agent Simulants. *Chem. Eur. J.* **2018**, *24*, 19208–19215. [CrossRef] [PubMed]

13. Jin, L.; Li, X.; Qi, Y.; Niu, P.; Zheng, S. Giant Hollow Heterometallic Polyoxoniobates with Sodalite-Type Lanthanide–Tungsten–Oxide Cages: Discrete Nanoclusters and Extended Frameworks. *Angew. Chem. Int. Ed.* **2016**, *55*, 13793–13797. [CrossRef] [PubMed]

14. Liao, G.; Gong, Y.; Zhang, L.; Gao, H.; Yang, G.; Fang, B. Semiconductor polymeric graphitic carbon nitride photocatalysts: The "holy grail" for the photocatalytic hydrogen evolution reaction under visible light. *Energy Environ. Sci.* **2019**, *12*, 2080–2147. [CrossRef]

15. Fu, J.; Yu, J.; Jiang, C.; Cheng, B. g-C_3N_4-Based Heterostructured Photocatalysts. *Adv. Energy Mater.* **2017**, *8*, 1701503. [CrossRef]

16. Yin, W.; Bai, L.; Zhu, Y.; Zhong, S.; Zhao, L.; Li, Z.; Bai, S. Embedding Metal in the Interface of a p-n Heterojunction with a Stack Design for Superior Z-Scheme Photocatalytic Hydrogen Evolution. *ACS Appl. Mater. Interfaces.* **2016**, *8*, 23133–23142. [CrossRef] [PubMed]

17. Xue, F.; Liu, M.; Cheng, C.; Deng, J.; Shi, J. Localized NiS_2 Quantum Dots on g-C_3N_4 Nanosheets for Efficient Photocatalytic Hydrogen Production from Water. *ChemCatChem* **2018**, *10*, 5441–5448. [CrossRef]

18. Zhang, C.; Zhou, Y.; Bao, J.; Fang, J.; Zhao, S.; Zhang, X.; Chen, S. Structure regulation of ZnS@g-C_3N_4/TiO_2 nanospheres for efficient photocatalytic H_2 production under visible-light irradiation. *Chem. Eng. J.* **2018**, *346*, 226–237. [CrossRef]

19. Zhang, R.; Niu, S.; Zhang, X.; Jiang, Z.; Zheng, J.; Guo, C. Combination of experimental and theoretical investigation on Ti-doped gC_3N_4 with improved photo-catalytic activity. *Appl. Surf. Sci.* **2019**, *489*, 427–434. [CrossRef]

20. Zhang, H.; Li, S.; Lu, R.; Yu, A. Time-Resolved Study on Xanthene Dye-Sensitized Carbon Nitride Photocatalytic Systems. *ACS Appl. Mater. Interfaces* **2015**, *7*, 21868–21874. [CrossRef]

21. Li, X.; Bi, W.; Zhang, L.; Tao, S.; Chu, W.; Zhang, Q.; Luo, Y.; Wu, C.; Xie, Y. Single-Atom Pt as Co-Catalyst for Enhanced Photocatalytic H_2 Evolution. *Adv. Mater.* **2016**, *28*, 2427–2431. [CrossRef] [PubMed]

22. Raziq, F.; Sun, L.; Wang, Y.; Zhang, X.; Humayun, M.; Ali, S.; Bai, L.; Qu, Y.; Yu, H.; Jing, L. Synthesis of Large Surface-Area g-C_3N_4 Comodified with MnO_x and Au-TiO_2 as Efficient Visible-Light Photocatalysts for Fuel Production. *Adv. Energy Mater.* **2018**, *8*, 1701580. [CrossRef]

23. Liu, M.; Jiao, Y.; Qin, J.; Li, Z.; Wang, J. Boron doped C_3N_4 nanodots/nonmetal element (S, P, F, Br) doped C_3N_4 nanosheets heterojunction with synergistic effect to boost the photocatalytic hydrogen production performance. *Appl. Surf. Sci.* **2020**, *541*, 148558. [CrossRef]

24. Zhou, X.; Zhao, D.; Li, X.; Sun, Y.; Zheng, S. Synthesis of noble-metal-free ternary $K_7HNb_6O_{19}$/$Cd_{0.5}Zn_{0.5}S$/g-C_3N_4 tandem heterojunctions for efficient photocatalytic performance under visible light. *Appl. Organomet. Chem.* **2019**, *33*, e5178. [CrossRef]

25. Yan, G.; Feng, X.; Xiao, L.; Xi, W.; Tan, H.; Shi, H.; Wang, Y.; Li, Y. Tuning of the photocatalytic performance of g-C_3N_4 by polyoxometalates under visible light. *Dalton Trans.* **2017**, *46*, 16019–16024. [CrossRef]

26. Wu, J.; Liao, L.; Yan, W.; Xue, Y.; Sun, Y.; Yan, X.; Chen, Y.; Xie, Y. Polyoxometalates Immobilized in Ordered Mesoporous Carbon Nitride as Highly Efficient Water Oxidation Catalysts. *ChemSusChem* **2012**, *5*, 1207–1212. [CrossRef]

27. Liu, J.; Xie, S.; Geng, Z.; Huang, K.; Fan, L.; Zhou, W.; Qiu, L.; Gao, D.; Ji, L.; Duan, L.; et al. Carbon Nitride Supramolecular Hybrid Material Enabled HighEfficiency Photocatalytic Water Treatments. *Nano Lett.* **2016**, *16*, 6568–6575. [CrossRef]

28. Long, Z.; Zhou, Y.; Chen, G.; Ge, W.; Wang, J. C_3N_4-$H_5PMo_{10}V_2O_{40}$: A dual-catalysis system for reductant-free aerobic oxidation of benzene to phenol. *Sci. Rep.* **2014**, *4*, 3651. [CrossRef] [PubMed]

29. Liu, M.; Chen, H.; He, Y.; Zhao, H.; Wang, R.; Zhang, L.; You, W. Biomolecule-mediated hydrothermal synthesis of polyoxoniobate–CdS nanohybrids with enhanced photocatalytic performance for hydrogen production and RhB degradation. *Dalton Trans.* **2017**, *46*, 9407–9414. [CrossRef]

30. Gan, Q.; Shi, W.; Xing, Y.; Hou, Y. A Polyoxoniobate/g-C_3N_4 Nanoporous Material with High Adsorption Capacity of Methylene Blue from Aqueous Solution. *Front. Chem.* **2018**, *6*, 7–16. [CrossRef]

31. Liu, C.; Feng, Y.; Han, Z.; Sun, Y.; Wang, X.; Zhang, Q.; Zou, Z. Z-scheme N-doped $K_4Nb_6O_{17}$/g-C_3N_4 heterojunction with superior visible-light-driven photocatalytic activity for organic pollutant removal and hydrogen production. *Chin. J. Catal.* **2021**, *42*, 164–174. [CrossRef]

32. Filowitz, M.; Ho, R.K.; Klemperer, W.G.; Shum, W. ^{17}O Nuclear Magnetic Resonance Spectroscopy of Polyoxometalates. 1. Sensitivity and Resolution. *Inorg. Chem.* **1979**, *18*, 93–103. [CrossRef]

33. Martin, D.J.; Qiu, K.; Shevlin, S.A.; Handoko, A.D.; Chen, X.; Guo, Z.; Tang, J. Highly Efficient Photocatalytic H_2 Evolution from Water using Visible Light and Structure-Controlled Graphitic Carbon Nitride. *Angew. Chem. Int. Ed.* **2014**, *53*, 9240–9245. [CrossRef] [PubMed]

34. Lin, B.; Yang, G.; Yang, B.; Zhao, Y. Construction of Novel Three Dimensionally Ordered Macroporous Carbon Nitride for Highly Efficient Photocatalytic Activity. *Appl. Catal. B Environ.* **2016**, *198*, 276–285. [CrossRef]

35. Heng, S.; Li, L.; Li, W.; Li, H.; Pang, J.; Zhang, M.; Bai, Y.; Dang, D. Enhanced Photocatalytic Hydrogen Production of the Polyoxoniobate Modified with RGO and PPy. *Nanomaterials* **2020**, *10*, 2449. [CrossRef]

36. Heng, S.; Song, Q.; Liu, S.; Guo, H.; Pang, J.; Qu, X.; Bai, Y.; Li, L.; Dang, D. Construction of 2D polyoxoniobate/RGO heterojunction photocatalysts for the enhanced photodegradation of tetracycline. *Appl. Surf. Sci.* **2021**, *553*, 149505. [CrossRef]

37. Bi, J.; Zhu, L.; Wu, J.; Xu, Y.; Wang, Z.; Zhang, X.; Han, Y. Optimizing electronic structure and charge transport of sulfur/potassium co-doped graphitic carbon nitride with efficient photocatalytic hydrogen evolution performance. *Appl. Organomet. Chem.* **2019**, *33*, e5163. [CrossRef]

38. Wang, K.; Li, Q.; Liu, B.; Cheng, B.; Ho, W.; Yu, J. Sulfur-doped g-C_3N_4 with enhanced photocatalytic CO_2-reduction performance. *Appl. Catal. B Environ.* **2015**, *176–177*, 44–52. [CrossRef]

39. Black, J.R.; Nyman, M.; Casey, W.H. Rates of Oxygen Exchange between the $[H_xNb_6O_{19}]^{8-x}_{(aq)}$ Lindqvist Ion and Aqueous Solutions. *J. Am. Chem. Soc.* **2006**, *128*, 14712–14720. [CrossRef]

40. Xing, W.; Tu, W.; Han, Z.; Hu, Y.; Meng, Q.; Chen, G. Template-induced high-crystalline g-C_3N_4 nanosheets for enhanced photocatalytic H_2 evolution. *ACS Energy Lett.* **2018**, *3*, 514–519. [CrossRef]

41. Zhang, J.; Wei, M.; Wei, Z.; Pan, M.; Su, C. Ultrathin Graphitic Carbon Nitride Nanosheets for Photocatalytic Hydrogen Evolution. *ACS Appl. Nano Mater.* **2020**, *3*, 1010–1018. [CrossRef]

42. Zhang, J.; Zhang, M.; Zhang, G.; Wang, X. Synthesis of Carbon Nitride Semiconductors in Sulfur Flux for Water Photoredox Catalysis. *ACS Catal.* **2012**, *2*, 940–948. [CrossRef]

43. Kong, Y.; Lv, C.; Zhang, C.; Chen, G. Cyano group modified g-C_3N_4: Molten salt method achievement and promoted photocatalytic nitrogen fixation activity. *Appl. Surf. Sci.* **2020**, *515*, 146009. [CrossRef]

44. Zhao, C.; Chen, Z.; Xu, J.; Liu, Q.; Xu, H.; Tang, H.; Li, G.; Jiang, Y.; Qu, F.; Lin, Z.; et al. Probing supramolecular assembly and charge carrier dynamics toward enhanced photocatalytic hydrogen evolution in 2D graphitic carbon nitride nanosheets. *Appl. Catal. B Environ.* **2019**, *256*, 117867. [CrossRef]

45. Li, Y.; Yang, M.; Xing, Y.; Liu, X.; Yang, Y.; Wang, X.; Song, S. Preparation of Carbon-Rich g-C_3N_4 Nanosheets with Enhanced Visible Light Utilization for Efficient Photocatalytic Hydrogen Production. *Small* **2017**, *13*, 1701552. [CrossRef]

46. Aureliano, M.; Ohlin, C.A.; Vieira, M.O.; Marques, M.P.; Caseye, W.H.; Carvalho, L.B. Characterization of decavanadate and decaniobate solutions by Raman spectroscopy. *Dalton Trans.* **2016**, *45*, 7391–7399. [CrossRef]

47. Jiang, J.; Ou-yang, L.; Zhu, L.; Zheng, A.; Zou, J.; Yi, X.; Tang, H. Dependence of electronic structure of g-C_3N_4 on the layer number of its nanosheets: A study by Raman spectroscopy coupled with first-principles calculations. *Carbon.* **2014**, *80*, 213–221. [CrossRef]

48. Dong, H.; Guo, X.; Yang, C.; Ouyang, Z. Synthesis of g-C_3N_4 by different precursors under burning explosion effect and its photocatalytic degradation for tylosin. *Appl. Catal. B Environ.* **2018**, *230*, 65–76. [CrossRef]

49. Xiao, T.; Tang, Z.; Yang, Y.; Tang, L.; Zhou, Y.; Zou, Z. In situ construction of hierarchical WO_3/g-C_3N_4 composite hollow microspheres as a Z-scheme photocatalyst for the degradation of antibiotics. *Appl. Catal. B Environ.* **2018**, *220*, 417–428. [CrossRef]

50. Butler, M.A. Photoelectrolysis and physical properties of the semiconducting electrode WO_3. *J. Appl. Phys.* **1977**, *48*, 1914. [CrossRef]

51. Nekoueia, F.; Nekoueib, S.; Pouzeshc, M.; Liu, Y. Porous-CdS/Cu_2O/graphitic-C_3N_4 dual p-n junctions as highly efficient photo/catalysts for degrading ciprofloxacin and generating hydrogen using solar energy. *Chem. Eng. J.* **2020**, *385*, 123710. [CrossRef]

52. Wang, Y.; Bayazit, M.K.; Moniz, S.J.; Ruan, Q.; Lau, C.; Martsinovich, N.; Tang, J. Linker-controlled polymeric photocatalyst for highly efficient hydrogen evolution from water. *Energy Environ. Sci.* **2017**, *10*, 1643–1651. [CrossRef]

53. Cao, S.; Huang, Q.; Zhu, B.; Yu, J. Trace-level phosphorus and sodium co-doping of g-C_3N_4 for enhanced photocatalytic H_2 production. *J. Power Sources* **2017**, *351*, 151–159. [CrossRef]

54. Lia, H.; Wang, Z.; Lua, Y.; Liu, S.; Chen, X.; Wei, G.; Ye, G.; Chen, J. Microplasma electrochemistry (MIPEC) methods for improving the photocatalytic performance of g-C_3N_4 in degradation of RhB. *Appl. Surf. Sci.* **2020**, *531*, 147307. [CrossRef]

55. Cai, S.; Wang, L.; Heng, S.; Li, H.; Bai, Y.; Dang, D. Interaction of Single-Atom Platinum–Oxygen Vacancy Defects for the Boosted Photosplitting Water H_2 Evolution and CO_2 Photoreduction: Experimental and Theoretical Study. *J. Phys. Chem. C* **2020**, *124*, 24566–24579. [CrossRef]

56. Low, J.; Yu, J.; Jaroniec, M.; Wageh, S.; Al-Ghamdi, A.A. Heterojunction photocatalysts. *Adv. Mater.* **2017**, *29*, 1601694. [CrossRef]

57. Wang, Z.; Tan, H.; Chen, W.; Li, Y.; Wang, E. A copper (II)–ethylenediamine modified polyoxoniobate with photocatalytic H_2 evolution activity under visible light irradiation. *Dalton Trans.* **2012**, *41*, 9882. [CrossRef]

58. Geng, Q.; Liu, Q.; Ma, P.; Wang, J.; Niu, J. Synthesis, crystal structure and photocatalytic properties of an unprecedented arsenic-disubstituted Lindqvist-type peroxopolyoxoniobate ion: $\{As_2Nb_4(O_2)_4O_{14}H_{1.5}\}^{4.5-}$. *Dalton Trans.* **2014**, *43*, 9843. [CrossRef]

59. Niu, J.; Li, F.; Zhao, J.; Ma, P.; Zhang, D.; Ulrich Kortz, B.B.; Wang, J. Tetradecacobalt(II)-Containing 36-Niobate $[Co_{14}(OH)_{16}(H_2O)_8Nb_{36}O_{106}]^{20-}$ and Its Photocatalytic H_2 Evolution Activity. *Chem. Eur. J.* **2014**, *20*, 9852–9857. [CrossRef]

60. Shen, J.; Zhang, Y.; Zhang, Z.; Li, Y.; Gao, Y.; Wang, E. Polyoxoniobate-based 3D framework materials with photocatalytic hydrogen evolution activity. *Chem. Commun.* **2014**, *50*, 6017. [CrossRef]

61. Hu, J.; Wang, Y.; Zhang, X.; Chi, Y.; Yang, S.; Li, J.; Hu, C. Controllable Assembly of Vanadium-Containing Polyoxoniobate-Based Three-Dimensional Organic–Inorganic Hybrid Compounds and Their Photocatalytic Properties. *Inorg. Chem.* **2016**, *55*, 7501–7507. [CrossRef] [PubMed]